Assessment of global variations in the velocity–porosity relationship of marine sediments and rocks using the legacy data of scientific ocean drilling programs

Yuya Akamatsu

Research Institute for Marine Geodynamics, Japan Agency for Marine-Earth Science and Technology, Kanagawa, Japan

---

This manuscript has been submitted for publication in Geochemistry, Geophysics, Geosystems. Please note the manuscript has yet to be formally accepted for publication. Subsequent versions of this manuscript may have slightly different content. If accepted, the final version of this manuscript will be available via the 'Peer-reviewed Publication DOI' link on the right-hand side of this webpage.

Abstract

The physical properties of sediments and rocks are routinely measured during scientific ocean drilling programs, as such data enable the recovered materials to be linked to geophysical observations and provide constraints on subseafloor lithology. However, lithological descriptions are not consistently linked to physical properties datasets for older drilling expeditions, thereby limiting global assessments of trends in lithology-dependent physical properties across various tectonic settings. In this study I compiled publicly available physical property data collected onboard, including the lithology-labeled datasets of recent expeditions, and developed a machine learning model to assign broad lithological context to unlabeled samples. Lithological labels were simplified into six classes: biogenic/carbonate sediment, siliciclastic sediment, volcaniclastic sediment, basaltic rock, gabbroic rock, and ultramafic rock. A bagged decision tree model was trained using porosity, bulk density, grain density, P-wave velocity, and magnetic susceptibility, and was applied to unlabeled data. The model achieved an overall accuracy of ~83% on the test dataset. Results shows that global trends in velocity–porosity relationships vary with lithology and show large internal variability. Applying a linear mixed-effects model, which statistically separates systematic effects shared across the dataset from group-specific variability, the deviations from the global trend are attributed primarily to variations between drilling areas and heterogeneity within each drilling area, rather than the tectonic setting. These results demonstrate that regional geological processes and local heterogeneity should be considered when utilizing physical property data for modeling and interpreting geophysical structures.

Plain Language Summary

Scientific ocean drilling has produced a large archive of sediment and rock samples from beneath the seafloor. The physical properties of these samples, including porosity and P-wave velocity, are routinely measured during drilling expeditions and provide important constraints on subseafloor materials through comparison with geophysical observations. However, many older records lack labels describing the lithology, which limits comprehensive evaluations of the lithology-dependence of physical properties across diverse tectonic settings. This study employed a machine learning approach that combines available lithology-labeled data with unlabeled records of physical properties. The model correctly predicted broad lithological classes in ~83% of test cases. The combined records identified lithology-dependent global trends in relationships between P-wave velocity and porosity, although considerable scatter and deviations from the global trend remained within each lithology. The scatter is attributed in part to the tectonic setting; however, most of the observed variability is associated with differences among drilling sites, as well as smaller-scale heterogeneity within individual drilling sites. These results demonstrate that integrated datasets of physical properties can provide useful first-order constraints on the lithology of unlabeled records from legacy ocean drilling projects, while emphasizing the need to consider the regional geological context when interpreting petrophysical and geophysical data.

Key Points

- Physical properties of marine sediment and rock reveal global trends in velocity–porosity relationships across diverse tectonic settings.
- A machine learning model trained on lithology-labeled datasets successfully predicted lithologies for older unlabeled datasets.
- Scatter about the global trends within each lithology mainly reflects regional-scale variability rather than the tectonic setting.

1 Introduction

Scientific ocean drilling has provided a unique archive of subseafloor materials and associated shipboard data through decades of international drilling programs, including the Deep Sea Drilling Program (DSDP), the Ocean Drilling Program (ODP), and the Integrated Ocean Drilling Program/International Ocean Discovery Program (IODP). Over the course of more than 400 expeditions, these programs have recovered enormous amounts of drillcore from diverse oceanographic, tectonic, and sedimentary settings. These cores and data have been used to address a wide range of scientific questions, including the history of Earth's climate and oceans (Littler et al., 2019; Lowery et al., 2019), the structure and dynamics of the oceanic lithosphere (Arculus et al., 2019; Neal et al., 2019), the nature of the deep biosphere (D'Hondt et al., 2019; Heuer et al., 2019), and geohazards associated with earthquakes (Fulton et al., 2019). With the ongoing transition to a new phase of international scientific ocean drilling, the International Ocean Drilling Programme ($IODP^3$), marked by the retirement of the drilling vessel *JOIDES Resolution* and an increasing emphasis on programs that utilize legacy cores, the scientific value of archived cores and shipboard datasets is becoming increasingly important (Koppers & Coggon, 2020). These archives provide not only a record of past drilling but also a reusable resource for testing new hypotheses using modern analytical, computational, and data-science approaches.

Measurements of the physical properties of rock and sediment are among the most fundamental datasets that are routinely acquired during scientific ocean drilling. Properties such as porosity, density, and P-wave velocity provide quantitative constraints on the composition, pore structure, alteration state, and consolidation of recovered materials (Blackman et al., 2019; Christensen & Salisbury, 1975; Erickson & Jarrard, 1998; Hoffman & Tobin, 2004; Le Ber et al., 2022; e.g., Lee et al., 2021; Violay et al., 2010). These measurements are also essential for linking core-scale observations to geophysical observations, because they control how lithological and structural variations are expressed in geophysical data, including seismic velocity, density, and magnetic structures. As such, shipboard physical property data are widely used to interpret geophysical data when seeking to understand subsurface structures and processes (e.g., Akamatsu et al., 2026; Carlson, 2010; Swift et al., 2008; Tsuji et al., 2008).

Despite their broad availability, shipboard physical property data have not been fully integrated across ocean drilling expeditions in a form that allows a systematic comparison among lithologies, depths, and geological settings. Previous studies have compiled and interpreted physical property data for specific regions, lithologies, or tectonic environments, but global-scale integration across ODP and IODP records remains limited. One major obstacle is that physical property datasets and lithological descriptions are not consistently available in a unified format across different drilling programs and expedition eras. Recent compilations, such as the LILY database (Childress et al., 2024), have made important progress by linking physical property measurements with lithological descriptions for recent IODP expeditions. However, comparable lithology-linked datasets are not consistently available for early ODP and IODP expeditions, even though physical property measurements are commonly accessible through public databases. Lithological information is generally reported only in expedition reports or post-cruise publications and is not available as structured database tables that are linked directly to other datasets, including measurements of physical properties. This hinders the quantitative reuse of legacy ocean drilling data, particularly because trends in physical properties are strongly controlled by lithology and cannot be interpreted solely as a function of depth or tectonic setting.

To extend lithological context to older datasets, this study employed a machine learning approach that combines available lithology-labeled dataset with unlabeled physical property records. First, I compile publicly available shipboard physical property data from ODP and IODP expeditions and harmonize them into a unified dataset. The focus is on routinely measured properties, including porosity, bulk density, grain density, P-wave velocity, and magnetic susceptibility, and their relationships are evaluated across major lithological groups and geological settings. To assign a lithological class to samples without structured lithology labels, a bagged decision tree classifier was trained using the LILY database (Childress et al., 2024), in which physical property measurements are linked to lithological descriptions. The trained model is then applied to unlabeled ODP/IODP physical property data to predict broad lithological groupings. Using this integrated dataset, I examine global trends in the physical properties of sediments and rocks, and statistically assess how these trends depend on lithology and tectonic setting. This approach enables a comparison of petrophysical relationships across a much broader range of materials and environments than is possible from individual expeditions alone.

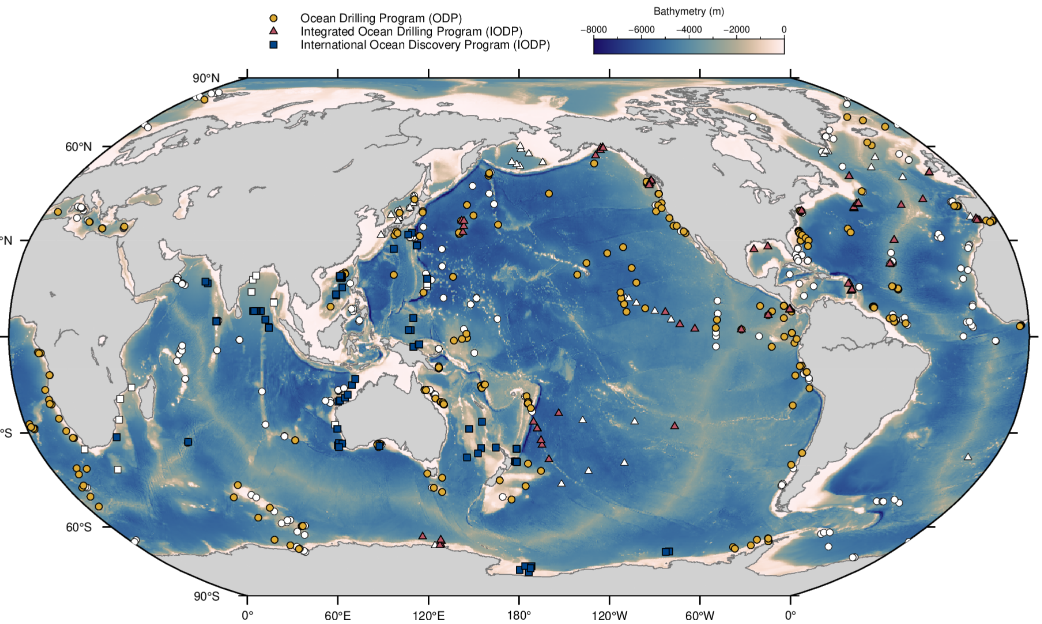

Figure 1 Locations of drill sites used for the physical property analysis. Open symbols indicate sites from which physical property data were compiled but were excluded from the present analysis because of incomplete measurements or insufficient data quality.

This study provides a framework for reusing legacy ocean drilling data in combination with data-driven techniques, thereby supporting future core–log–seismic integration, geophysical interpretation, and strategic use of archived cores.

2 Materials and methods

2.1 Data sources

A global dataset of physical properties was compiled using data obtained from 798 scientific ocean drilling sites during 155 ODP/IODP expeditions (Figure 1). The dataset includes ODP Legs 100–210 and IODP Expeditions 301–379.

For IODP expeditions since Expedition 318, physical property data are available through the LILY database compiled by Childress et al. (2024). The LILY database utilized the core descriptions logged using the software programs DescLOgik or GEODESC since 2009 and provides lithological information linked directly to the physical property measurements. This makes it particularly suitable for investigating lithology-dependent variations in the physical properties of sediments and rocks (Svadlenak et al., 2026). For the ODP and early IODP expeditions, physical property data were compiled from the Janus database, which is archived online. For these expeditions, however, lithological descriptions are available only in expedition reports rather than as a structured database, making systematic linkage between physical properties and lithology difficult. Given this background, the present study utilized the physical properties and lithology data obtained during later IODP expeditions to establish a machine learning model to predict the lithology of unlabeled dataset obtained during ODP/IODP expeditions. I also incorporated data obtained by the ICDP (International Continental Drilling Program) Oman Drilling Project (Kelemen et al., 2020) to improve the representation of ultramafic rocks, as described in detail in the section 2.3.

From these databases, I compiled data on the following physical properties: porosity, bulk density, grain density, P-wave velocity, magnetic susceptibility, natural gamma radiation (NGR), thermal conductivity, and shear strength. Density and porosity data are derived through MAD (moisture and density) measurements that quantify mass and volume on ~8cm^3 specimens extruded from the split core. P-wave velocity is measured in various ways during expeditions. Here I used data measured on split core section (PWS) and discrete core samples (PWC). The magnetic susceptibility represents the degree to which a material can be magnetized in an external magnetic field, and is also measured in various ways. Here I used MSL data obtained with the multisensor track system that automatically measures the physical properties of whole-round core sections. These magnetic susceptibility data were measured in instrumental units (IU) rather than SI units and were used as originally reported, including minus values. NGR is the total-gamma ray emissions produced by the decay of radioisotopes within core samples, and can be used to estimate the lithology of a formation through estimates of K, U, and Th contents. NGR is measured on the multisensor track system with MSL data, although it was not measured prior to Leg 150. Thermal conductivity is a bulk material property that governs the rate of heat transfer through a material, and is used to determine heat flow, along with temperature measurements. During expeditions, thermal conductivity is usually measured on whole-round cores for sediment samples and split core sections for consolidated sediment and rocks samples using various types of probes. Shear strength tests can be performed with several different devices; this study used data obtained using the automated vane shear (AVS) system. These physical properties were measured according to standard ODP/IODP protocols. The detailed methodologies are described in the IODP laboratory manuals (Blum, 1997).

2.2 Data standardization and quality control

The data on physical properties were compiled from all expeditions for which the relevant measurements were available. Measurement names and units were then standardized to ensure consistency among datasets. Because most physical properties were measured at different depths, direct comparisons were not possible. Therefore, depth matching was performed using the MAD measurements as the reference. For each MAD measurement, only data acquired within 10 cm of the MAD depth were retained, thereby enabling direct comparisons among the physical properties. When multiple measurements were available within the same depth interval, their average value was used. In addition, NGR data acquired before ODP Leg 169 were excluded because their values are systematically higher than those from later expeditions, likely due to differences in measurement conditions.

We then extracted samples with complete measurements for the physical properties used to construct the machine learning model. The model was trained using porosity, bulk density, grain density, P-wave velocity, and magnetic susceptibility because these properties are both widely available and strongly dependent on lithology. Although NGR is useful in distinguishing the lithology, it was excluded because it was not routinely measured before

ODP Leg 150, which would substantially reduces the number of available datasets. After removing samples with missing values, 120,193 rows of data remained in the dataset.

Next, I performed data cleaning and standardization. Firstly, samples with physically unrealistic values were removed, including negative porosities, porosities exceeding 100%, and density or P-wave velocity values outside the expected ranges of values for water and common rock-forming minerals. I then utilized submethods of MAD measurements to identify poor-quality density and porosity data, because MAD measurements have generally employed three different submethods (A–C) throughout the ODP/IODP program, resulting in substantial differences in data quality. Submethod C, which is the standard protocol of current IODP expeditions, measures the sample volume after the specimen has been sufficiently dried. Submethods A and B determine the sample volume using a water-saturated specimen, which may lead to overestimation of the bulk and grain densities by as much as 10% (Blum, 1997). Although the use of these data is thus not recommended, I applied a quality control procedure to retain as many reliable samples as possible and maximize the size of the dataset. A reference envelope based on submethod C data was defined in the bulk density, porosity, and grain density data space using the k-Nearest Neighbors (kNN) algorithm, and submethod A/B data falling inside the envelope were flagged (Figure S1). Some data from submethods A and B are within the reference envelope; however, these methods produced systematically high densities in the low bulk-density regime (<2.4 g/cm^3), as suggested by the IODP protocols (Blum, 1997). In contrast, submethod A/B data at higher bulk densities (2.4 g/cm^3) largely overlapped with the reference envelope. These results probably reflect the fact that samples with a high bulk density have low porosity, so that errors in mass and volume measurements have a small influence on the density and porosity. I therefore retained submethod A/B data that fell within the reference envelope and the high bulk-density domain in which method-dependent offsets were negligible, while excluding measurements from the low-density domain. This filtering reduced the dataset to 28,386 rows, because nearly half of the ODP/IODP MAD data were acquired using submethods A or B.

After these quality-control procedures, scatter plots of the physical properties still contained apparent outliers. To identify and remove these data, the Local Outlier Factor (LOF) algorithm was applied, which detects anomalies based on the local density of observations relative to neighboring samples. It was assumed that 3% of the dataset consists of outliers and the detected samples were removed, resulting in a final dataset of 27,625 rows (Figure 2).

2.3 Lithological classification

To construct the machine learning model, lithology labels for the IODP dataset were first defined for the training dataset. Because the lithological descriptions reported in the LILY database are highly diverse, they were simplified into a manageable number of classes suitable for machine learning. I therefore grouped the data into six lithological classes (biogenic/carbonate sediment, siliciclastic sediment, volcaniclastic sediment, basaltic rock, gabbroic rock, and ultramafic rock) based on the reported principal lithology, prefixes, suffixes, degree of consolidation, and lithology subtype (Table S1).

The biogenic/carbonate sediment class consists mainly of diatom ooze, nannofossil ooze, and lithified carbonate rocks. The siliciclastic sediment class includes predominantly silty,

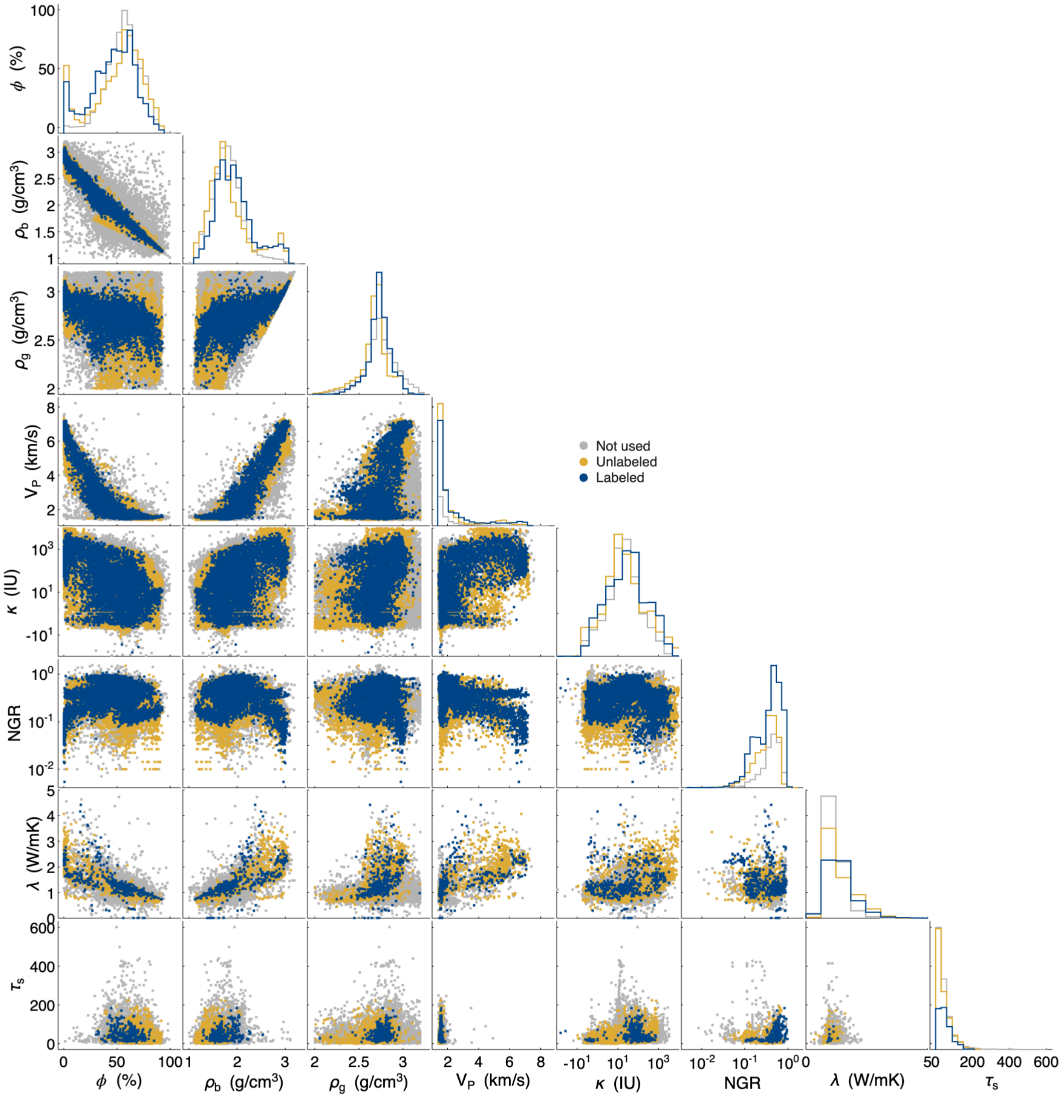

Figure 2 Scatter plot matrix of the physical properties of ODP/IODP legacy data. Blue and yellow dots denote data with and without lithology labels, respectively, while gray dots denote data excluded from the analysis because of low data quality. Magnetic susceptibility is shown in instrumental units (IU) and displayed using a symmetric logarithmic transformation. ϕ is porosity, ρ_{b} is bulk density, ρ_{g} is grain density, V_{P} is P-wave velocity, κ is magnetic susceptibility, NGR is natural gamma radiation, λ is thermal conductivity, and τ_{s} is shear strength.

sandy, and muddy sediment regardless of their degree of consolidation. The volcaniclastic sediment class comprises mainly tuffaceous and ashy sediment, lapilli, volcanic breccia, and hyaloclastite. The basaltic rock class includes primarily lava flows and pillow lavas. Boninites were also assigned to this class because they are a typical component of the upper crust in forearc settings. Therefore, the basaltic class should be regarded not as a geochemical definition of basalt, but rather as a representative class of extrusive rocks that make up the upper oceanic crust. The gabbroic rock class includes gabbro, olivine gabbro, troctolite, and even dolerite (diabase), and should therefore be regarded as representing intrusive mafic rocks of the lower crust.

These five classes account for 99.7% of the LILY dataset, and ultramafic rocks are only sparsely represented in the LILY database. However, serpentinized peridotites were recovered during earlier drilling expeditions that targeted oceanic core complexes and serpentinite seamounts (Michibayashi et al., 2019), meaning that ultramafic rocks are an important lithology class to be predicted. Thus, the training dataset was supplemented with physical property measurements from the ICDP (International Continental Drilling Program) Oman Drilling Project (Kelemen et al., 2020). The additional data consist of 535 serpentinized peridotite samples and 90 gabbroic samples recovered from the BA and CM sites, where the mantle section and crust–mantle transition zones of the Oman ophiolite were drilled, respectively. These samples were used exclusively for model training and were not included in the subsequent analyses of lithology-dependent variations in physical properties. The remaining 0.5% of samples were grouped as “other” and excluded from subsequent analyses.

After the depth matching and quality-control procedures described above, the labeled dataset comprised 7269 rows. The final labeled dataset consists of 31.9% biogenic/carbonate sediment, 32.3% siliciclastic sediment, 13.2% volcaniclastic sediment, 10.2% basaltic rock, 5.0% gabbroic rock, and 7.4% ultramafic rock. These labeled data span nearly the full range of variations in physical properties observed in the unlabeled ODP/IODP dataset, thereby supporting the applicability of the classifier, although predictions outside the training-domain envelope should be interpreted with caution (Figure 2).

2.4 Machine learning prediction of lithology

We developed a machine learning model to classify lithological groups from physical property predictors. The primary predictors were porosity, bulk density, grain density, P-wave velocity, and magnetic susceptibility. In addition to these measured variables, three derived ratio variables were included: porosity divided by P-wave velocity, grain density divided by P-wave velocity, and grain density divided by porosity. These variables were added to help the model capture relative relationships among porosity, density, and velocity that might distinguish lithological groups. The labeled dataset was randomly divided into training (80% of the data) and test datasets (20%). The prediction model was developed using a bagged decision tree classifier, in which the ensemble consists of multiple decision trees trained on bootstrap-resampled subsets of the training data. This approach was selected because it can represent nonlinear classification boundaries and interactions among physical property predictors while remaining relatively interpretable. The model outputs posterior probability estimates (herein, the class score) for each lithological class. The predicted lithology was assigned according to the class with the highest score. Model performance was also evaluated using class-wise precision, recall, and F1 scores, in addition to the overall confusion matrix. The 'precision' measures the reliability of samples assigned to a given class, the 'recall' measures how completely samples of that class were recovered, and the F1 score summarizes the balance between precision and recall.

3 Results and discussion

3.1 Prediction results

Figure 3 shows the confusion matrix obtained for the test dataset. Most of the samples were correctly classified along the diagonal of the confusion matrix, indicating that the model successfully captured the major differences between the lithological classes. The overall prediction accuracy is high (82.7).

For sedimentary classes, some off-diagonal components are present, resulting in precision, recall, and F1 scores ranging from 76% to 85%. These metrics suggest that the sediments are generally classified well, although some misclassifications occur between biogenic/carbonate and siliciclastic sediments and between siliciclastic and volcaniclastic sediments. This misclassification results from the similar physical properties among these lithologies and likely reflects the mixed nature of marine sediments, which commonly contain variable proportions of siliciclastic, biogenic, carbonate, and volcaniclastic components. Such compositional mixing produces overlapping physical property distributions, making these lithologies more difficult to distinguish.

For basaltic, gabbroic, and ultramafic rocks, all performance metrics range from 80% to 96%, indicating that these lithologies can be classified with high reliability. Some basaltic rocks are misclassified as volcaniclastic sediments, likely because volcanic-derived sedimentary rocks (e.g., basaltic breccias and hyaloclastites) have similar physical properties to porous and altered basalts (Lee et al., 2021). Likewise, a few ultramafic rocks are misclassified as basaltic or gabbroic rocks, probably because weakly serpentinized peridotite has similar physical properties to massive mafic rocks (Miller & Christensen, 1997).

Using the model trained by the labeled dataset, I predicted the lithologies of samples in the unlabeled dataset comprising 20,943 rows. Of these, ~87% were classified as sediment and 13% as igneous rock. The predicted lithological proportions were 40.7% biogenic/carbonate sediment, 36.6% siliciclastic sediment, 9.65% volcaniclastic sediment, 7.39% basalt, 3.63% gabbro, and 2.03% ultramafic rock (Figure 4a).

Figure 4b shows the distribution of maximum class scores for each predicted lithology. Class scores of ~1.0 indicate high confidence in the prediction. The three sedimentary classes exhibit bimodal distributions, with peaks at ~1.0 and ~0.5. Samples with scores of ~0.5 have comparable probabilities across the three sedimentary classes. This is consistent with the results obtained for the test dataset, although a larger proportion of the unlabeled data exhibit low to moderate prediction confidence, reflecting the greater compositional diversity of marine sediments.

In contrast, the scores for basaltic rocks are concentrated at ~0.9, indicating high confidence in the predictions. Gabbroic rocks exhibit a sharp peak at a class score of ~1, together with a smaller peak at ~0.5, with most samples being concentrated near one of

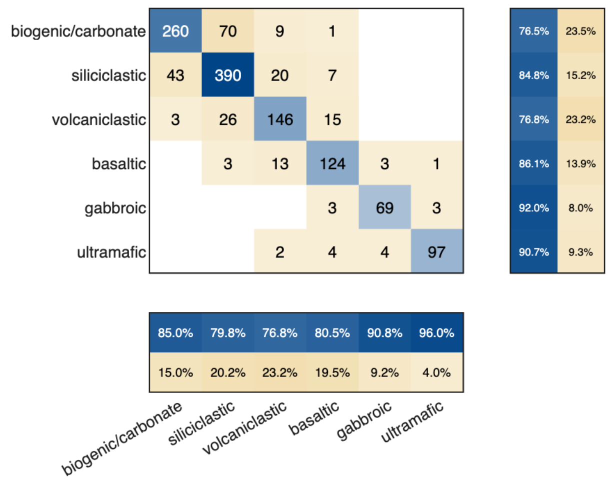

Figure 3 Confusion matrix showing the performance of the lithology prediction model on the test dataset. Rows correspond to the true lithology labels and columns to the predicted labels. Cell values indicate the number of samples, with darker colors representing larger counts. The percentages at right indicate the recall for each lithology class, whereas those at the bottom indicate the precision for each predicted class.

these modes. This distribution suggests that gabbroic rocks can usually be classified with high confidence, although a subset of samples is confused with other lithologies, most likely basaltic and ultramafic rocks. Ultramafic rocks also show a dominant peak at ~1, along with smaller peaks at 0.5 and ~0.8. This broader, multimodal distribution suggests that the physical properties of ultramafic rocks are partially similar to those of other lithological classes, making their prediction difficult.

3.2 Variations in physical properties with lithology

Figure 5 shows the distribution of physical properties for each lithology in both the labeled and unlabeled datasets. Although some outliers are present, both datasets exhibit similar lithology-dependent distributions of physical properties, suggesting that the trained model can be reliably applied to the unlabeled dataset.

Sediments have consistently high porosities, broadly ranging from 30% to 90%, with little variation among biogenic/carbonate, siliciclastic, and volcaniclastic sediments (Figure 5a). Basaltic rocks show a wide range of porosity (mainly 1%–40%), whereas gabbroic rocks have very low porosities, with median values below 1%. Ultramafic rocks exhibit intermediate porosities between those of basaltic and gabbroic rocks (mainly 1%–5%). Bulk density and P-wave velocity display the opposite trend with porosity (Figure 5b, d). Sediments have a consistently low bulk density (<2 g/cm^3) and P-wave velocity (<3 km/s), while igneous rocks have a higher bulk density (>2.4 g/cm^3) and velocity (>4 km/s), with gabbroic rocks having the highest values (up to ~3 g/cm^3 and ~7 km/s). Grain density also shows little variation among sediment types, while basaltic and gabbroic rocks generally have high grain densities (Figure 5c). Ultramafic rocks have grain densities comparable to those of the sedimentary lithologies, consistent with the relatively low density

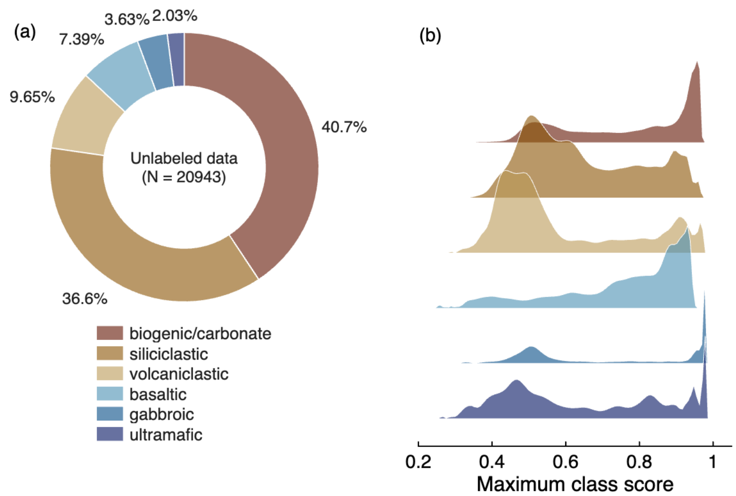

Figure 4 (a) Proportions of different lithologies predicted for the unlabeled dataset. (b) Distributions of the maximum class score for each predicted lithology.

of serpentine (~2.55 g/cm^3). In the unlabeled dataset, however, ultramafic rocks tend to exhibit higher grain densities than those in the labeled dataset. This difference may indicate that the unlabeled dataset contains a larger proportion of relatively fresh peridotites and/or that some damaged or altered gabbroic rocks, whose physical properties overlap with those of moderately serpentinized peridotites (Miller & Christensen, 1997), have been misclassified as ultramafic rocks.

The magnetic susceptibility varies substantially among sedimentary lithologies (Figure 5e). This likely reflects the presence of volcanic-derived magnetic minerals (e.g., magnetite) in siliciclastic and volcaniclastic sediments, indicating that magnetic susceptibility is an effective discriminator of sedimentary lithology. Igneous lithologies do not show clear differences in magnetic susceptibility. The high magnetic susceptibility of ultramafic rocks reflects magnetite formation during serpentinization (Fujii et al., 2016; Oufi et al., 2002).

To evaluate the reliability of predictions for the unlabeled dataset, the predicted lithologies were compared with core descriptions at several sites where the corresponding lithologies were recovered. As noted above, datasets in which physical property measurements can be directly matched to lithological descriptions are limited for the ODP and early IODP expeditions. Verification at the level of individual discrete samples is therefore difficult, and I instead assessed whether the predicted labels were consistent with the reported lithostratigraphic units.

Figure 6 shows depth variations in the maximum class scores. At Site 1085 off the western coast of Africa, where nannofossil ooze is the dominant lithology (Wefer et al., 1998), almost all data were classified as biogenic/carbonate sediment (Figure 6a). At Site 977 in the western Mediterranean, where the cores are described as consisting mainly of terrigenous turbiditic silty clay and sandstone (Comas et al., 1996), siliciclastic sediment was frequently predicted (Figure 6b). At Site 1201 in the middle of Philippine Sea, the recovered cores consist of sediments containing abundant volcaniclastic material with underly-

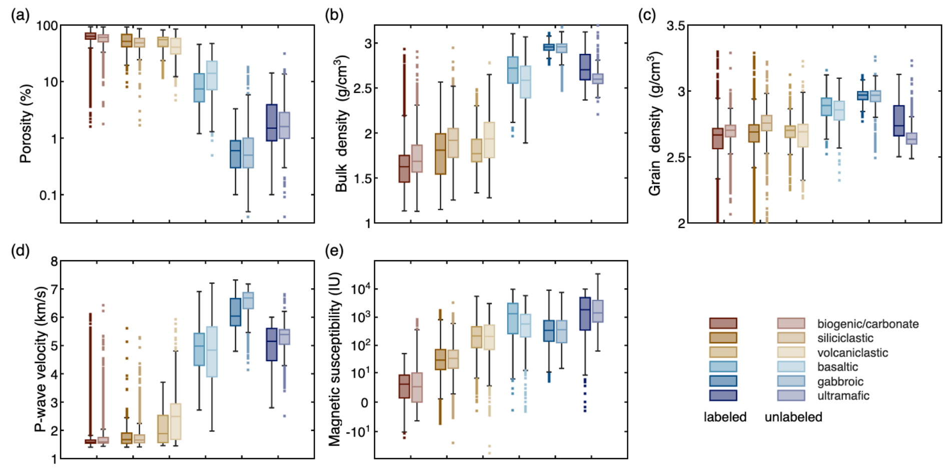

Figure 5 Box-and whisker plots of (a) porosity, (b) bulk density, (c) grain density, (d) P-wave velocity, and (d) magnetic susceptibility. The dark and light colors represent the labeled dataset and the unlabeled dataset with the predicted lithologies, respectively. Boxplots show the median (center line), interquartile range (box), and whiskers extending to 1.5 times the interquartile range; points represent outliers. Magnetic susceptibility is shown in instrumental units (IU) and includes negative values; therefore, it is displayed using a symmetric logarithmic transformation.

ing basaltic basement (Salisbury et al., 2002), in agreement with the predicted lithologies (Figure 6c). At Site 1256, which penetrated the oceanic crust into the gabbroic section on the flank of the mid-ocean ridge in the eastern Pacific (Teagle et al., 2006), the lithology is predicted to transition from basaltic to gabbroic at deeper levels (Figure 6d), consistent with the documented lithological transition from lava to sheeted dikes. At Site 920, where serpentinized mantle rocks exposed on the seafloor were recovered from an ocean core complex at the Mid-Atlantic Ridge, the predictions indicate a predominance of ultramafic rocks.

The predicted lithologies for the unlabeled dataset are broadly consistent with the reported lithostratigraphic units, indicating that lithology can be successfully classified from physical property data. However, as suggested by the validation results for the labeled dataset, the predictions likely include 10–20% misclassification owing to overlapping distributions of physical properties among lithologies. Although the low class scores of sediments may actually reflect their mixed nature (i.e., they contain a range of minerals), some misclassifications are evident at representative hard-rock drilling sites, where physical property measurements are directly linked to core lithologies. At these sites, some samples predicted to be basaltic, gabbroic, or ultramafic rocks with relatively low class scores of ~0.5 are inconsistent with the reported lithologies (e.g., ultramafic rocks at Site 1256 and basaltic rocks at Site 920). These cases indicate that some mafic and ultramafic rocks exhibit physical properties outside the typical ranges of their respective lithologies (Figure 5), likely owing to localized geological processes such as deformation and alteration. Consequently, accurate discrimination of these lithologies is difficult using the available physical property data alone. Therefore, the machine learning prediction should be regarded as a tool for broad lithological categorization of large datasets rather than for definitive lithological identification of individual samples. Accordingly, the predicted labels are used below to evaluate global lithology-dependent trends in physical properties, rather than to focus on individual sites for which a limited number of samples are available.

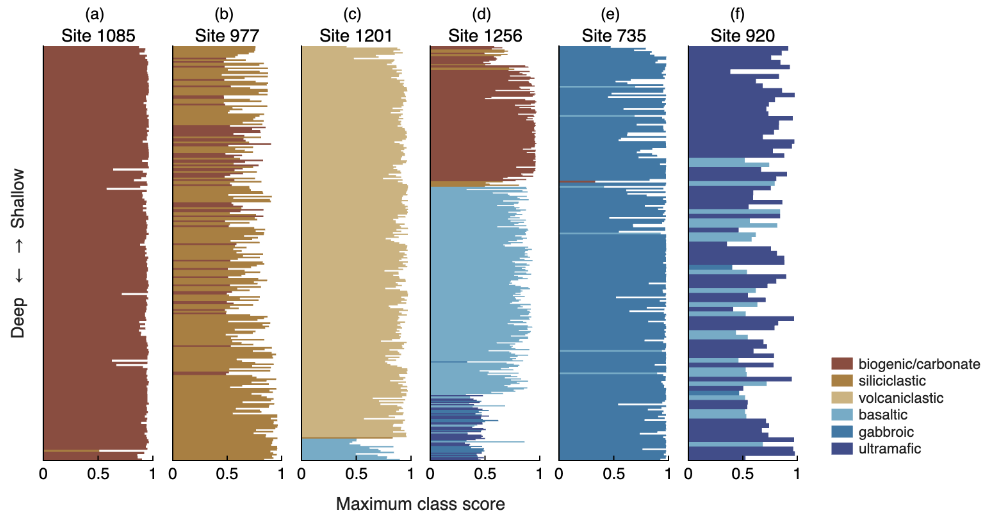

Figure 6 Depth variations in the predicted lithologies and their class scores at representative drilling sites. Vertical axes represent the data sorted by depth at each site but do not necessarily indicate their actual depths. Colors indicate the predicted lithology.

3.3 Global relationships between physical properties

The relationships among all physical properties for each lithology are summarized in Figure S2. Here, the focus is on the relationships between P-wave velocity, which is one of the most widely used geophysical parameters, and density and porosity, which are fundamental material properties.

Figure 7a–b shows the global relationship between P-wave velocity and bulk density. Although the bulk density generally increases with P-wave velocity, the relationship varies substantially among lithologies. Siliciclastic sediments exhibit a rapid increase in bulk density from approximately 1.1 to 2.4 g/cm^3 over a relatively narrow range of P-wave velocity from 1.5 to ~3.0 km/s. Biogenic/carbonate sediments shows a similar trend to siliciclastic sediments in this low-velocity range, although several samples exhibit higher velocities up to ~6 km/s.

Volcaniclastic sediments tend to have slightly lower bulk density at a given P-wave velocity. This is likely because such sediments can contain abundant clay minerals, such as smectite, whose interlayer water causes porosity measurements to be overestimated by up to 20%, thereby resulting in underestimation of the bulk density (Blum, 1997). Although the low bulk densities may partly reflect the intrinsically low grain density of clay minerals, caution is required when interpreting the density and porosity data of volcaniclastic sediments. Basaltic rocks show a relatively gentle increase in bulk density with P-wave velocity, with ultramafic rocks displaying a similar trend. Gabbroic rocks show little change in bulk density with increasing P-wave velocity.

These nonlinear relationships are broadly consistent with the empirical relationship proposed by Brocher (2005), which is a polynomial function for predicting the average crustal bulk density from P-wave velocity. However, this model does not reproduce the rapid increase in sediment density with P-wave velocity and tends to underestimate the bulk density in the range of velocity values for basaltic–gabbroic-ultramafic rocks (3–7 km/s). I therefore propose a new V_{P}–density relationship that is calibrated specifically for ocean drillcore data using a sixth-order polynomial, rather than the fifth-order polynomial proposed by Brocher (2005), as follows:

$$\rho_{\mathrm{b}} = -0.7181V_{\mathrm{P}} + 2.757V_{\mathrm{P}}^2 - 1.542V_{\mathrm{P}}^3 + 0.3725V_{\mathrm{P}}^4 - 0.04183V_{\mathrm{P}}^5 + 0.001787V_{\mathrm{P}}^6, \tag{1}$$

where ρ_{b} is the bulk density (g/cm^3) and V_{P} is the P-wave velocity (km/s). Note that volcaniclastic samples were excluded from the fitting because of the possibility of underestimation of bulk density, as discussed above.

The proposed relationship performs well in reproducing the rapid increase in sediment density and change in slope with increasing P-wave velocity up to ~7 km/s. Although biogenic/carbonate and siliciclastic sediments and basaltic and ultramafic rocks cannot be readily distinguished using this relationship, it can be used to identify broad transitions from sedimentary to igneous sequences beneath the seafloor on the basis of P-wave velocity and density structures estimated by geophysical investigations. However, considerable scatter remains around the fitted curve, indicating that P-wave velocity and bulk density cannot be uniquely related across all samples. Given that this scatter is unlikely to arise primarily from analytical error, deviations from the model probably reflect lithology-dependent or geological processes and the resulting variations in microstructures within the rock.

A clear correlation and lithological dependence are also identified between P-wave velocity and porosity (Figure 7c–d). P-wave velocity decreases with increasing porosity, although the rate of decrease varies among lithologies. Gabbroic and ultramafic rocks exhibit a steep decrease in P-wave velocity, with velocities reduced by 1–2 km/s at porosities below 5%. In contrast, basaltic rocks show a more gradual trend, with P-wave velocity decreasing by up to 3 km/s as porosity increases from 0% to 20%. Most biogenic/carbonate and siliciclastic sediments exhibit an even weaker dependence on porosity and follow nearly identical trends, whereas some samples show trends similar to that of basaltic rocks. Although volcaniclastic sediments tend to exhibit higher P-wave velocities than the other sediments at porosities of 20%–50%, this is likely an artifact of porosity overestimation caused by the presence of smectite, as discussed above.

The relationship between P-wave velocity and porosity depends primarily on the mineral assemblage, texture, consolidation state, and pore structure, all of which reflect the geological processes experienced by sediments and rocks. These factors are lithology-dependent and give rise to distinct velocity–porosity relationships and the variability observed within each lithology. Understanding the cause of these variations is therefore important for constraining lithology-dependent geological processes through the interpretation of seismic velocity observations. Because the governing mechanisms differ between sediments and rocks, in the following sections, we examine their velocity–porosity relationships of sediments and rocks separately using established empirical and theoretical models. Ultramafic rocks were excluded from the subsequent analyses because of the relatively low confidence in the predicted lithologies and the difficulty in modeliong their velocity–porosity relationships owing to the complex reaction processes that occur. during serpentinization (Akamatsu et al., 2025).

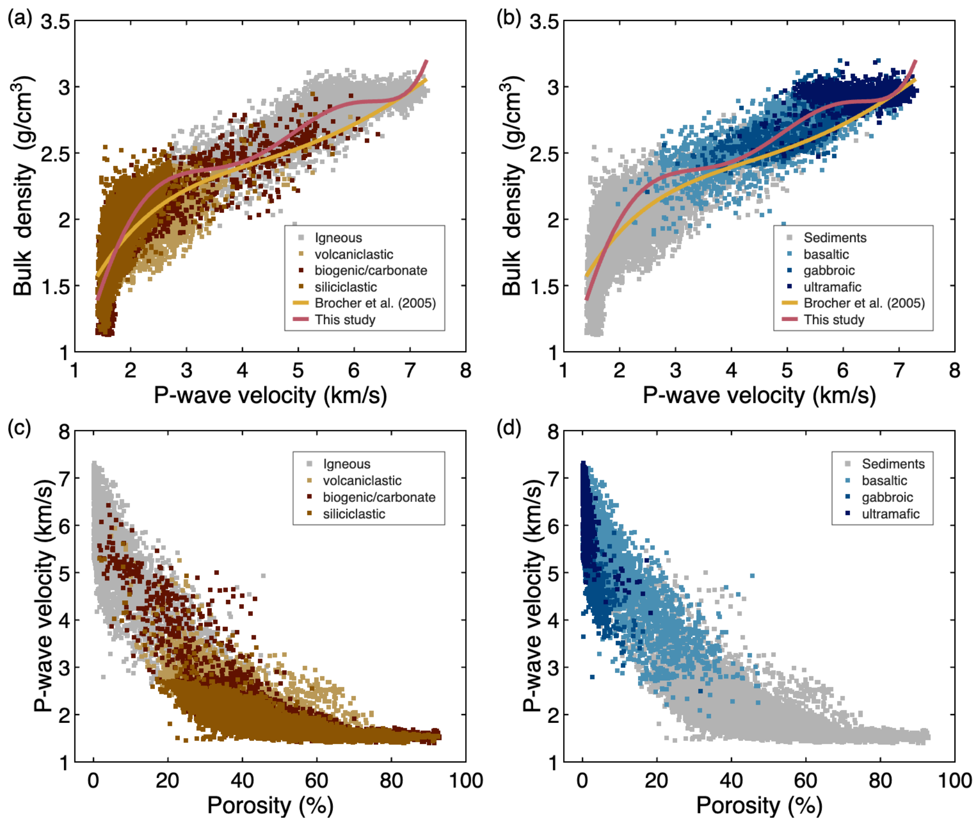

Figure 7 Global relationships between (a, b) P-wave velocity and bulk density and (c, d) P-wave velocity and porosity, for different lithological classes. The yellow and red curves in (a) and (b) represent the global empirical relationships proposed by Brocher (2005) and this study, respectively.

3.3.1 Velocity–porosity relationship of sediment

The velocity–porosity relationship of water-saturated sediment is commonly divided into two regimes separated by a critical porosity ϕ_c (Mavko et al., 2020; Nur et al., 1995). For porosities below ϕ_c, the mineral framework is load-bearing and the elastic wave velocity approaches that of the mineral framework. In contrast, when porosity exceeds ϕ_c, the material behaves as a suspension in which the pore fluid is the load-bearing phase, resulting in the elastic wave velocity approaching that of the pore fluid. The critical porosity is controlled by the mechanical framework of the constituent minerals and evolves in response to compaction history, stress conditions, and diagenetic processes.

Numerous models have been developed to reproduce the observed velocity–porosity relationship of marine sediment, although only a few models can describe the complete transition across the critical porosity continously. Among these, the empirical model of Erickson & Jarrard (1998) (herein the EJ model) is often used to fit the velocity–porosity relationship of marine sediment or to convert observed seismic velocity to porosity. In the EJ model, the velocity–porosity relationship depends on several parameters, as follows:

$$V_\mathrm{P} = A + B\phi + \frac{0.305}{(\phi - C)^2 + D} + E(f_\mathrm{sh} - F)[\tanh(G(\phi - \phi_\mathrm{c})) - |\tanh(G(\phi - \phi_\mathrm{c}))|], \quad (2)$$

where f_sh is the shale (clay) fraction and parameters A–G are constants. The parameters A–G and the critical porosity ϕ_c are used to distinguish the consolidation history between normal- and high-consolidation modes, reflecting differences in the sediment consolidation state and grain-framework stiffness. The high-consolidation mode represents more strongly compacted or tectonically compressed sediment, whereas the normal-consolidation mode represents sediment that primarily compacted as a result of normal burial. The shale fraction f_sh is between 0 and 1, with the porosity-free velocity (i.e., matrix velocity) when $f_\mathrm{sh} = 0$ corresponding to that of a clean sandstone matrix, whereas $f_\mathrm{sh} = 1$ represents a pure shale matrix. f_sh has commonly been replaced by the clay fraction in later studies to extend the model to a wider range of sediment types (e.g., Hoffman & Tobin, 2004; Jeppson & Kitajima, 2022).

Table 1 Parameters for calculating the EJ-type velocity–porosity relationship, as proposed by Jeppson and Kitajima (2022)

	Normal consolidation	High consolidation
A	0.739	1.11
B	0.552	0.178
C	0.13	0.135
D	0.0725	0.0775
E	1.103	1.1
F	1.07	0.985
G	7	8
ϕ_c	0.31[a]	0.48

[a] Modified from the original value of 0.48.

The EJ model provides a convenient and widely used empirical framework for describing velocity–porosity relationships in marine sediment. However, the original formulation contains multiple empirical parameters that are often strongly correlated, making parameter estimation sensitive to decisions regarding which parameters are fixed or optimized. This parameter non-uniqueness complicates the physical interpretation of the fitted parameters and hinders meaningful comparisons among different lithologies and geological settings. To address this issue, a mixed EJ model is introduced in which the predicted P-wave velocity is represented as a linear combination of the normal- and high-consolidation models, as follows:

$$V_\mathrm{P} = (1 - \psi)V_\mathrm{P}^\mathrm{normal} + \psi V_\mathrm{P}^\mathrm{high}, \quad (3)$$

where $V_\mathrm{P}^\mathrm{normal}$ and $V_\mathrm{P}^\mathrm{high}$ are the P-wave velocity predicted by the normal- and high-consolidation modes, respectively. The parameter ψ represents an interpolation between the two end-member modes, with $\psi = 0$ and $\psi = 1$ corresponding to the normal- and high-consolidation modes, respectively, and is therefore interpreted as an index of consolidation state rather than as the physical mixing fraction (Figure S3).

For both end-member models, I adopted the parameters modified from the original EJ model by Jeppson & Kitajima (2022), who extended the applicability of the model to carbonate-rich sediment (Table 1). Although they proposed a common value of $\phi_\mathrm{c} = 0.48$ for the modified normal- and high-consolidation models, I instead adopted the original value of $\phi_\mathrm{c} = 0.31$ from Erickson & Jarrard (1998) for the normal-consolidation model, so that the two end-member models explicitly represent different consolidation histories. The shale fraction f_sh and the condolidation index ψ were estimated by nonlinear least-squares optimization.

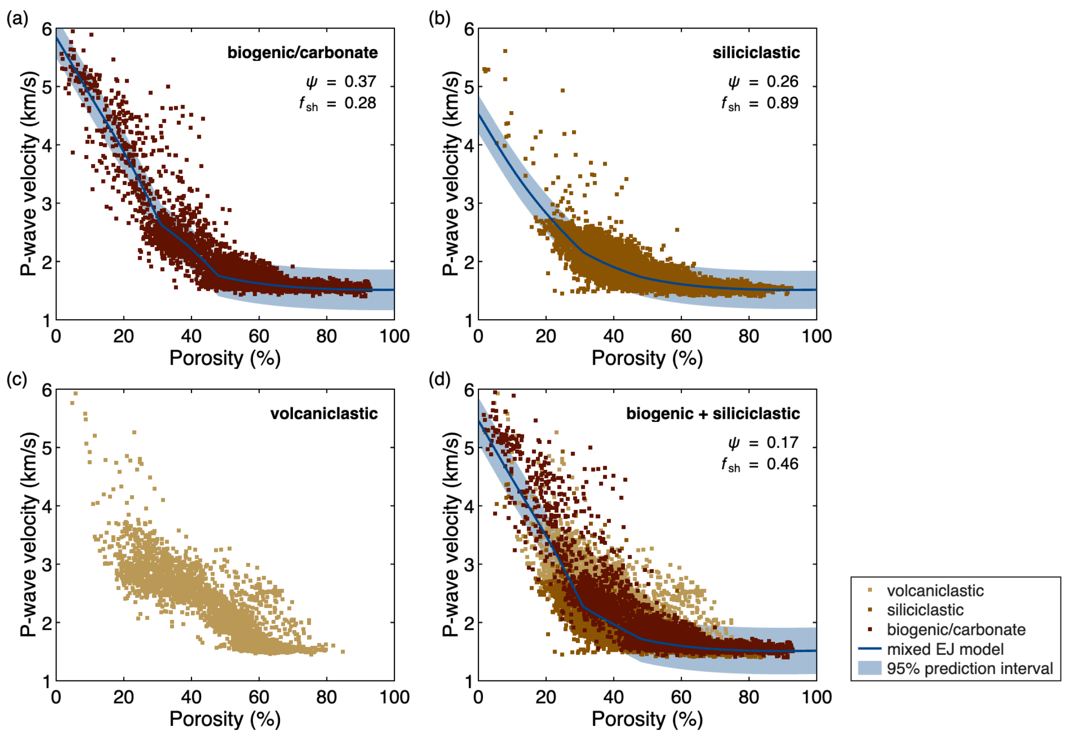

Figure 8 Relationship between porosity and P-wave velocity for (a) biogenic/carbonate sediment, (b) siliciclastic sediment, (c) volcaniclastic sediment, and (d) biogenic/carbonate and siliciclastic sediment. The blue line denotes the best-fit curve determined by the mixed model of Erickson and Jarrard (1998), and the shaded area indicates the 95% prediction interval. The optimized consolidation index and shale/clay fraction are shown for each lithology, except for volcaniclastic sediment.

The velocity–porosity relationships of biogenic/carbonate and siliciclastic sediments are well reproduced by the mixed EJ model, including the transition in slope across the critical porosity (Figure 8a–b). The estimated consolidation index values are similar between biogenic/carbonate and siliciclastic sediments, whereas the corresponding shale fraction is much higher for siliciclastic sediment. This indicates that the mechanism of compaction does not vary markedly between these lithologies, while siliciclastic sediments are composed largely of shale or clay.

Volcaniclastic sediment exhibits a different velocity–porosity trend to biogenic/carbonate and siliciclastic sediments, with the change in slope occurring at a porosity of 50%–60%, which is beyond the upper bound of the critical porosity in the mixed EJ model (Figure 8c). As discussed above, this shift is likely to reflect a systematic overestimation of porosity as a result of the presence of interlayer water in phyllosilicate minerals, (e.g., smectite). Therefore, volcaniclastic sediment was excluded from the subsequent analyses.

Despite the good agreement between the mixed EJ model and the global velocity–porosity relationship of biogenic/carbonate and siliciclastic sediments, considerable scatter remains around the fitted curve, similar to that observed in the density–velocity relationship (Figure 7a). These deviations likely reflect geological processes and the resulting variations in sediment texture, which may be expressed by variations in the model parameters.

To examine whether systematic deviations from the global trend are associated with the tectonic setting, each drilling site was assigned to a simplified tectonic setting, and the mixed EJ model was fitted separately for each category. The sites were classified into the following settings: active margin, forearc/accretionary prism, passive margin, oceanic crust, seamount/oceanic plateau, backarc, and other. Because passive margin and oceanic crust settings contain a wide range of porosity for both biogenic/carbonate and siliciclastic sediments, the two lithologies were fitted separately for these settings.

Figure 9 shows the velocity–porosity relationship and the corresponding mixed EJ model fit for each tectonic setting. For all settings, the mixed EJ model successfully reproduces the observed velocity–porosity relationship. The estimated consolidation index values and shale/clay fraction vary among tectonic settings and lithologies. Active margin and forearc/prism sediments exhibit relatively high consolidation index values of 0.52 and 0.76, respectively, even compared with other settings dominated by siliciclastic sediment (Figure 9a,d). These high values may reflect horizontal compression associated with plate subduction (Jarrard et al., 1995).

Passive margin sediment accounts for the majority of the dataset, and the fitted relationships for biogenic/carbonate and siliciclastic sediments are therefore nearly identical to the global trends, with a clear difference in shale/clay fraction between the two sediment classes. Although the difference is less pronounced in the passive margin setting, the other tectonic settings generally show slightly higher consolidation index values for biogenic/carbonate sediment than for siliciclastic sediment. This trend suggests that biogenic/carbonate sediment develops a load-bearing framework at relatively high porosity, possibly because early diagenetic cementation enables the sediment framework to become mechanically competent earlier than is the case for siliciclastic sediments (Jeppson & Kitajima, 2022).

Figure 10 shows the residuals between the measured P-wave velocities and those predicted by the global mixed EJ model (Figure 11d) for different tectonic settings. Although the mean residual remains close to zero across the entire porosity range, the scatter increases as the porosity decreases and varies among tectonic settings (Figure 10a).

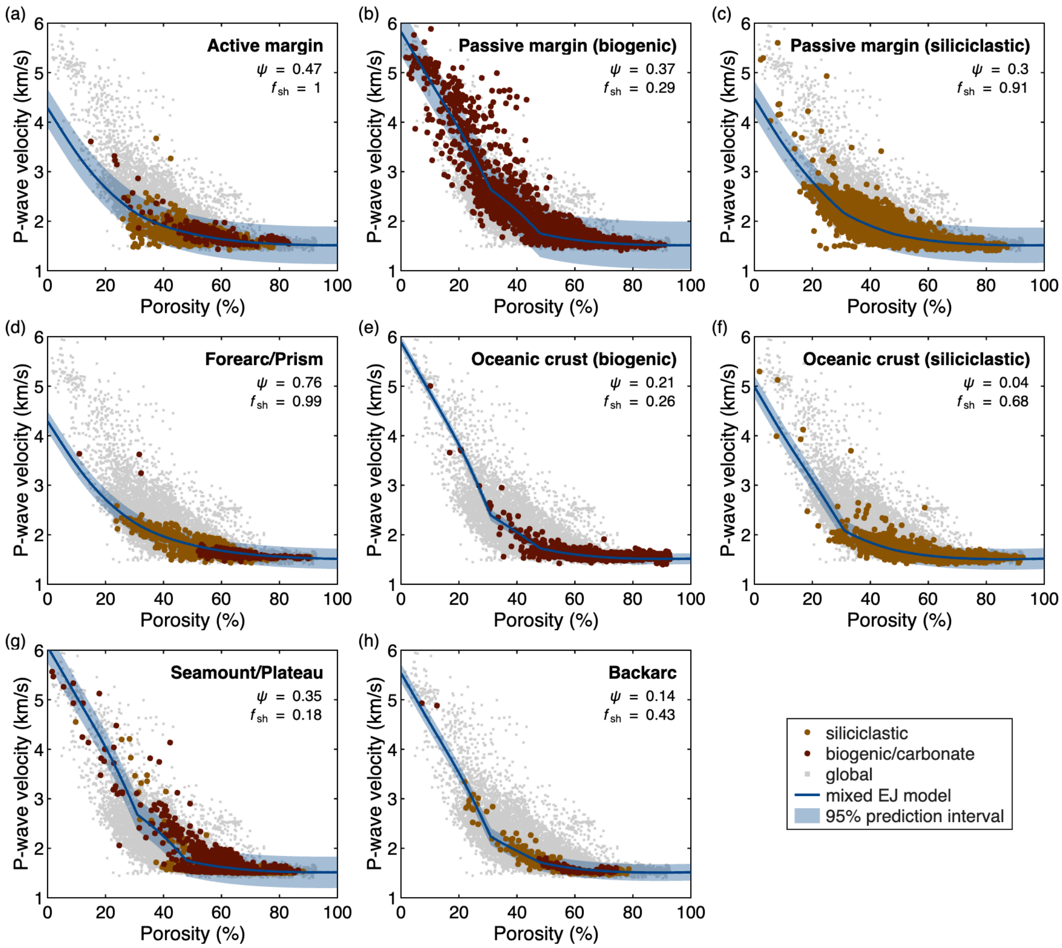

Figure 9 Relationship between porosity and P-wave velocity for biogenic/carbonate sediments and siliciclastic sediments for each tectonic setting. The blue line denotes the best-fit curve determined by the mixed EJ model, and the shaded area indicates the 95% prediction interval. The optimized consolidation index and shale/clay fraction are shown for each setting.

Below the critical porosity of the high-consolidation model (0.48), the residuals for the forearc/accretionary prism, backarc, and biogenic sediments from the oceanic crust are concentrated around zero (Figure 10b), indicating good agreement with the global trend, even though their estimated shale/clay fractions and consolidation index values differ from those of the global model. In contrast, siliciclastic sediments from passive margins and the oceanic crust exhibit systematic offsets from the global trend. Active margin and seamount/oceanic plateau sediments show bimodal residual distributions, indicating greater variability in the velocity–porosity relationship below the critical porosity than that predicted by the global model.

Although the residuals from the global velocity–porosity relationship show systematic differences among tectonic settings, substantial scatter remains within each setting (Figure 10c). This might be associated with different drilling expeditions, which results in the presence of systematic regional-scale variability for a given tectonic setting. I therefore applied a linear mixed-effects model (LMM) to discriminate the influence of the tectonic setting from regional-scale variability among expeditions. The LMM is designed to account for such hierarchical data structures by separating systematic effects shared across the dataset (fixed effects) from group-specific variability (random effects) (Nakagawa & Schielzeth, 2013). Porosity, lithology, and tectonic setting were treated as fixed effects, whereas expeditions were included as a random intercept (i.e., Exp-specific offset), allowing the mean residual velocity to vary among expeditions while estimating a common effect of tectonic setting across the dataset.

The fixed effects of porosity, lithology, and tectonic setting accounted for ~14% of the variance in the velocity residuals. Variance partitioning of the LMM indicates that porosity, lithology, and tectonic setting account for approximately 6%, 1%, and 7% of the total residual variance, respectively (Figure 10e). Thus, although the tectonic setting produces a systematic shift in the velocity–porosity relationship, it accounts for only a limited fraction of the total variability.

The estimated expedition-specific offsets are highly variable, ranging from –0.58 to 0.83 km/s (Figure 10c) and accounting for 40% of the total residual variance (Figure 10e). Thus, regional differences among expeditions represent a major source of variability even for a given tectonic setting. The remaining unexplained variance (~46%) may reflect geological heterogeneity at smaller spatial scales (Figure 10e), including differences among sites and individual samples, as well as compositional, diagenetic, and other geological factors that are not represented by the present classification. Therefore, these results indicate a hierarchical control on sediment velocity–porosity relationships, from the tectonic setting to regional geological conditions and finally local heterogeneity, thereby emphasizing the importance of understanding local geological processes when interpreting petrophysical and geophysical variability.

3.3.2 Velocity–porosity relationship of crustal rocks

The velocity-porosity relationship of igneous rocks is often linked to theoretical models based on effective medium theory, in which the elastic wave velocity of water-saturated rocks is controlled primarily by three factors: the intrinsic velocity of the solid phase (V_P^0), porosity, and pore geometry (e.g., Kachanov, 1994; Kuster & Toksöz, 1974; O'Connell & Budiansky, 1974; Takei, 2002). According to the differential effective medium (DEM)

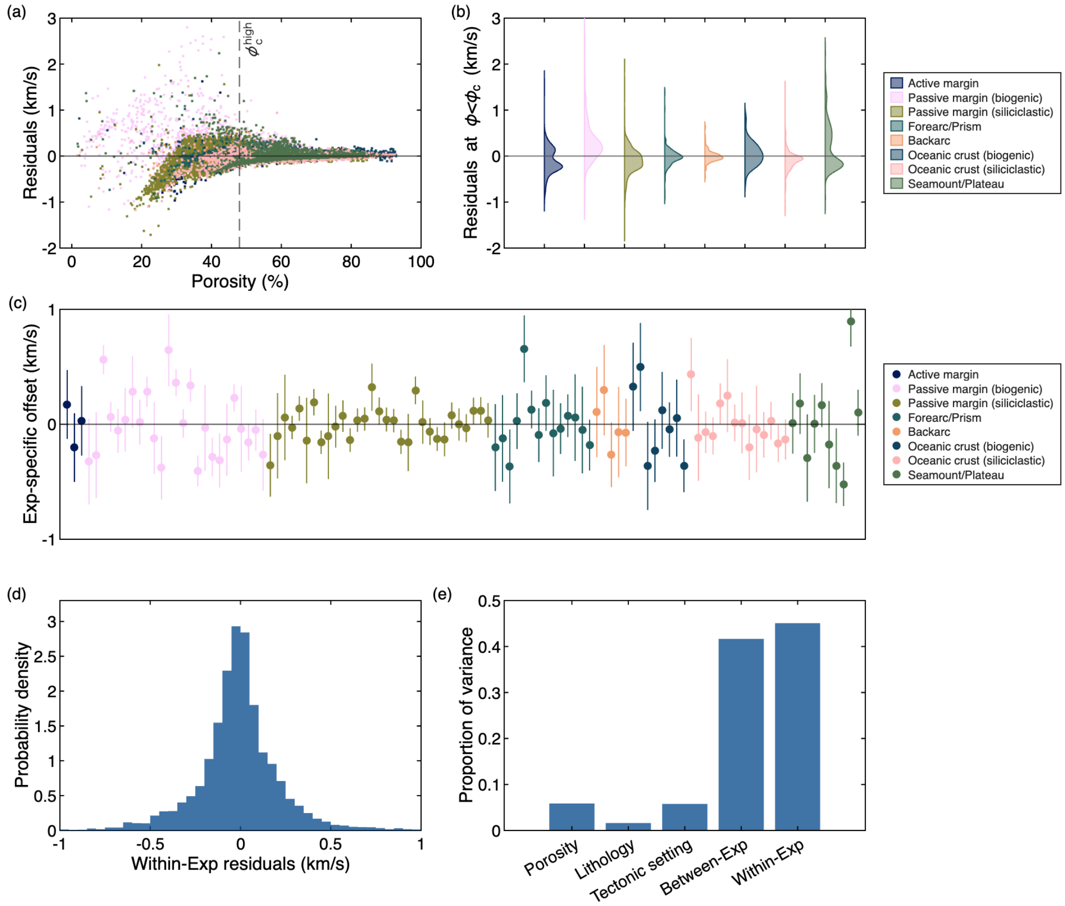

Figure 10 (a) Residuals between the measured P-wave velocities and those predicted by the global trend determined for biogenic/carbonate and siliciclastic sediments (Figure 8d) based on the mixed EJ model, with data colored by tectonic setting. (b) Distributions of the residuals for each tectonic setting at porosities below the critical porosity (0.48) for the high consolidation mode. (c) Offsets from the global trend for each expedition (intercepts of random effect) estimated by the linear-mixed effect model, colored by the tectonic setting. Vertical lines denote the 95% confidential interval. (d) Probability density function of residuals remaining after accounting for the effects of lithology, tectonic setting, and expedition-specific offsets. (e) Proportion of the variance explained by each effect relative to the total variance.

model (Berryman et al., 2002; Mavko et al., 2020), which models two-phase composites by incrementally adding the inclusion to the background, the effective bulk modulus K^* and shear modulus μ^* of an isotropic rock containing randomly oriented spheroidal pores saturated with fluid can be calculated as follows:

$$(1-\phi)\frac{d}{d\phi}[K^*(\phi)] = (K_i - K^*(\phi))\,P^*(\phi),$$

$$(1-\phi)\frac{d}{d\phi}[\mu^*(\phi)] = (\mu_i - \mu^*(\phi))\,Q^*(\phi),$$

with initial conditions $K^*(0) = K_0$ and $\mu^*(0) = \mu_0$; where K_0 and μ_0 are the bulk and shear moduli of the porosity-free material, respectively; K_i and μ_i are the bulk and shear moduli of the pore-filling phase, respectively; and ϕ is the porosity. P^* and Q^* are the volumetric and deviatoric strain concentration factors for a spheroidal pore, respectively, which are described as follows:

$$P^* = \frac{K^* + \frac{4}{3}\mu_i}{K_i + \frac{4}{3}\mu_i + \pi\alpha\beta^*},$$

$$Q^* = \frac{1}{5}\left[1 + \frac{8\mu^*}{4\mu_i + \pi\alpha(\mu^* + 2\beta^*)} + \frac{2K_i + \frac{4}{3}(\mu_i + \mu^*)}{K_i + \frac{4}{3}\mu_i + \pi\alpha\beta^*}\right],$$

$$\beta^* = \mu^*\frac{3K^* + \mu^*}{3K^* + 4\mu^*},$$

where α is the mean pore aspect ratio defined as $\alpha = w/c$, with c and w being the mean pore radius and aperture, respectively. These equations predict that the slope of the porosity–velocity relationship is dependent on the pore aspect ratio, with a small pore aspect ratio (i.e., thin crack) reducing the velocity at a relatively small porosity. The bulk and shear moduli of a porosity-free rock can be determined by assuming a $V_\mathrm{P}/V_\mathrm{S}$ value. Here, it is assumed that the typical $V_\mathrm{P}/V_\mathrm{S}$ of a porosity-free basaltic and gabbroic rock is 1.8 (Akamatsu et al., 2023; Hatakeyama et al., 2021) and the estimated the porosity-free velocity V_P^0 and mean pore aspect ratio α were estimated by nonlinear least-squares optimization.

Figure 11 shows the relationship between the porosity and P-wave velocity of basaltic and gabbroic rocks, with the best-fit curve determined by the DEM model. The DEM model successfully reproduces the distinct trends between basaltic and gabbroic rocks, with a higher porosity-free velocity and smaller pore aspect ratio for the. latter. The low aspect ratio estimated for gabbroic rocks (0.03) suggests that the pore structure of such rocks is dominated by thin cracks, consistent with aspect ratios previously estimated for the dike section of Hole 504B (Carlson, 2010). Although these thin cracks contribute little to the total porosity, they can substantially reduce the effective elastic stiffness of the rock, resulting in the steep slope of the V_P–porosity relationship. In contrast, the higher aspect ratios of basaltic rocks suggest the presence of stiffer, spherical pores or equant voids in addition to thin cracks. These more equant pores can substantially increase porosity without strongly reducing the stiffness of the rock framework, resulting in a lower sensitivity of V_P to porosity and thus a gentler V_P–porosity slope. These differences may arise from contrasting emplacement conditions (extrusive versus intrusive) as well as differences in the extent of post-emplacement brittle deformation.

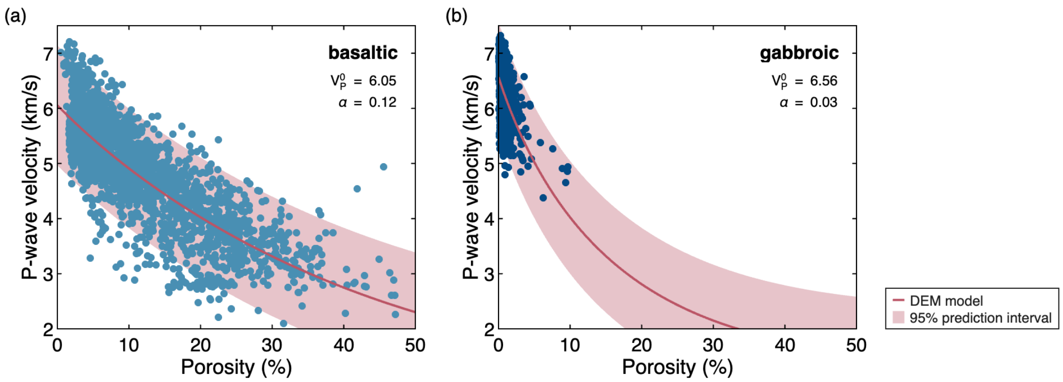

Figure 11 Relationship between the porosity and P-wave velocity for (a) basaltic and (b) gabbroic rocks. The red line denotes the best-fit curve determined by the differential effective medium model, and the shaded area indicates the 95% prediction interval. The optimized porosity-free velocity and mean pore aspect ratio are shown for each lithology.

The variations in V_P^0 primarily reflects variations in the elastic properties of the solid matrix (i.e., the mineral assemblage). The estimated V_P^0 values for basaltic and gabbroic rocks are lower than the typical V_P^0 of mafic rocks with primary minerals (~7 km/s). This might reflect the formation of secondary minerals during low-temperature hydrothermal alteration, as the elastic moduli of these minerals are much lower than those of primary minerals (Carlson, 2014). The lower V_P^0 of basaltic rocks may reflect more extensive low-temperature seawater alteration of extrusive rocks at shallower crustal levels, resulting in a greater abundance of secondary alteration minerals with a lower elastic modulus.

As with the sediments, the V_P–porosity relationship of crustal rocks exhibits considerable scatter about the global model. This scatter is particularly pronounced for basaltic rocks, with deviations of up to ~2 km/s across the entire porosity range. Such variability likely reflects variations in pore geometry and mineral assemblage, which are controlled mainly by geological processes within the upper oceanic crust.

To evaluate whether the tectonic setting has a systematic influence on these deviations from the global trend, the velocity–porosity relationship was again fitted separately for each simplified tectonic setting using the DEM model and subsequently the residuals from the global trend were evaluated. The fitting was performed for basaltic rocks recovered from backarc, forearc/accretionary prism, passive margin, mid-ocean ridge (MOR) flank and ocean basin, incoming plate, and seamount and oceanic plateau settings. Samples predicted to be basaltic rocks from the sites of ocean core complexes were excluded from this analysis because some of these samples might actually represent altered gabbroic or ultramafic rocks with similar physical properties to those of basaltic rocks.

Figure 13 shows the V_P–porosity relationships for basaltic rocks and the corresponding DEM model fits for each tectonic setting. The estimated pore aspect ratios vary little among tectonic settings and are broadly consistent with that of the global trend. In contrast, V_P^0 shows greater variability: backarc and incoming plate settings exhibit slightly lower values of ~5.6 km/s, whereas seamounts and oceanic plateaus show a higher value of 6.67 km/s. These differences may reflect variations in the extent of low-temperature

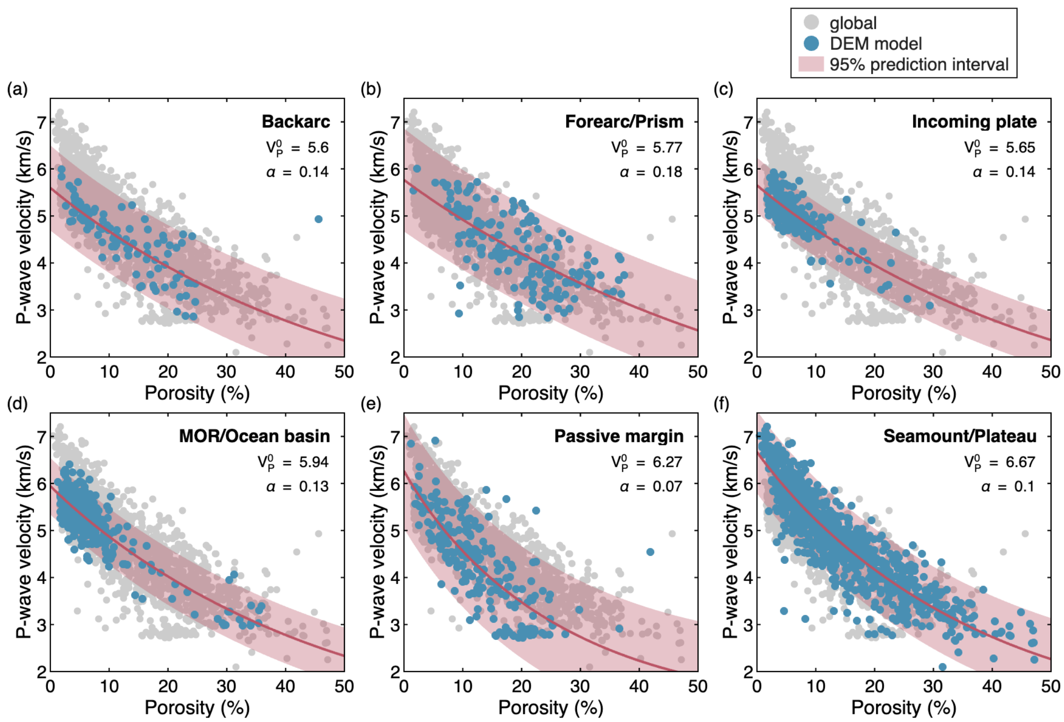

Figure 12 Relationship between the porosity and P-wave velocity for basaltic rock for each tectonic setting. The red line denotes the best-fit curve determined by the differential effective medium model, and the shaded area indicates the 95% prediction interval. The optimized values of the porosity-free velocity and mean pore aspect ratio are shown for each tectonic setting.

hydrothermal alteration among tectonic settings, with basaltic rocks from backarc and incoming plate settings experiencing intense hydrothermal alteration. A slightly lower aspect ratio is estimated for passive margin settings, possibly because mafic rocks recovered from passive margins may have an intrusive origin.

However, these estimates are based on the model that assumes a single pore geometry, whereas natural rocks may contain both cracks and vesicles with different aspect ratios that affect elastic wave velocity and porosity differently (e.g., Cheng & Toksöz, 1979; Tsuji & Iturrino, 2008; Wang et al., 2026). Accounting for multiple pore geometries could substantially change the estimated V_P^0. Therefore, the observed differences among tectonic settings cannot necessarily be attributed solely to variations in V_P^0 or the degree of alteration.

The differences among tectonic settings are also evident in the residuals from the global trend. Basaltic rocks from backarc and incoming plate settings tend to exhibit slightly lower V_P than the global trend, whereas those from forearc and seamount/oceanic plateau settings tend to exhibit higher values. However, variance partitioning using the LMM model indicates that the tectonic setting accounts for only ~5% of the residual variance, with most of the variance (~70%) being attributed to differences among expeditions. Thus, although the tectonic setting produces a systematic shift in the V_P–porosity relationship, the regional geological characteristics of individual drilling areas have a much greater influence. Approximately 22% of the residual variance also occurs within individual expeditions, suggesting an additional contribution from core-scale heterogeneity. These results indicate that, although the tectonic setting of basaltic rocks has a measurable influence on the velocity–porosity relationships, the regional geological context and smaller-scale heterogeneity must also be considered when interpreting petrophysical and geophysical variability.

3.4 Limitations and Perspectives

In this study, I compiled data on the physical properties of sediments and rocks from previous ODP/IODP expeditions and developed a machine learning model to predict the lithology from the physical properties using data with known lithological labels. Applying the trained model to the unlabeled dataset revealed distinct physical property trends among lithologies, enabling a statistical evaluation of the factors controlling the physical properties of sediments and crustal rocks. The machine learning model developed in this study achieved an overall prediction accuracy of ~80%, indicating that the presence of misclassified samples. The lithological classification scheme itself also has room for improvement. Developing more geologically distinctive and meaningful lithological classes could improve the accuracy of lithology prediction from physical properties and provide a more robust assessment of lithological controls on petrophysical variability. Integrating physical properties with geochemical and petrological information (e.g., geochemical and mineralogical data), would be particularly useful in developing such classifications and may ultimately enable geological processes, including diagenesis, alteration, and magmatic processes, to be better constrained from geophysical observations (Akamatsu et al., 2026).

In addition to improving the predictive model, assigning lithological labels directly to currently unlabeled data is still important. Lithological information for these data is available in textual descriptions and images from visual core descriptions (VCDs). Multimodal

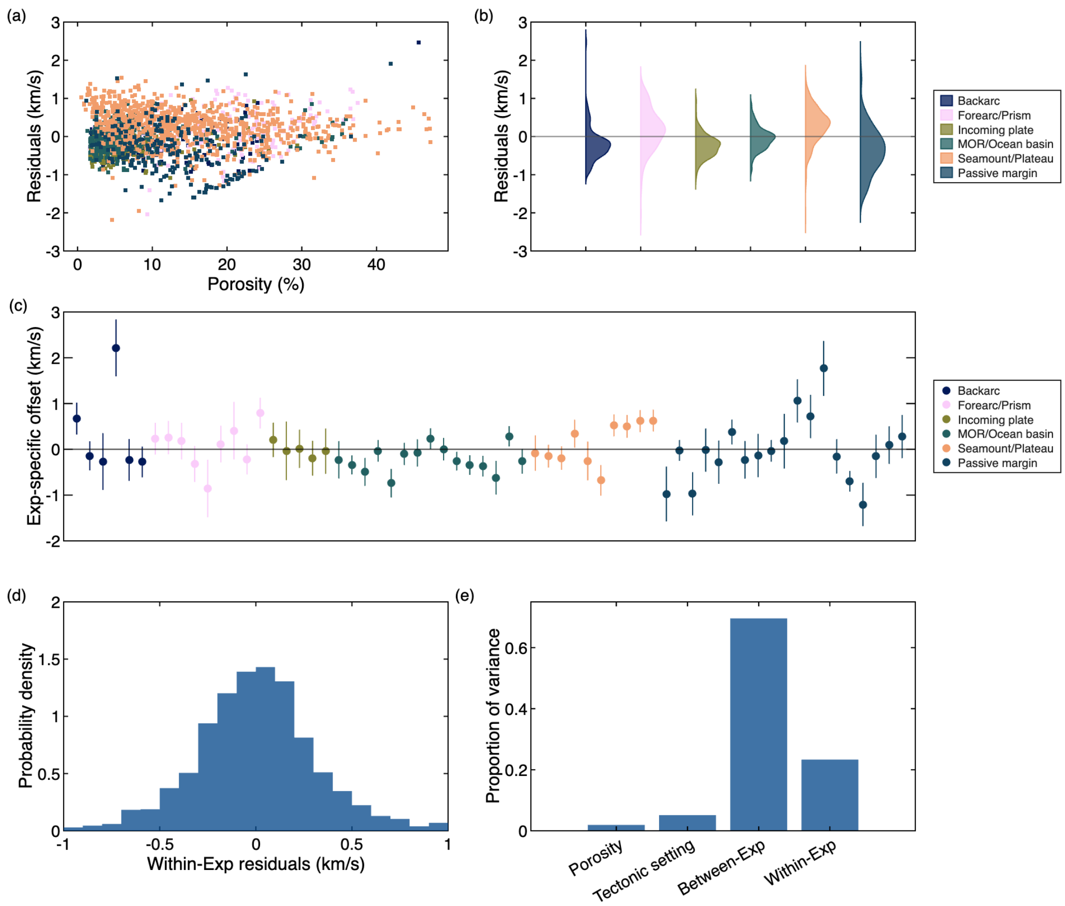

Figure 13 (a) Residuals between the measured P-wave velocities and those predicted by the global trend determined for basaltic rock (Figure 11a) based on the differential effective medium model, with data colored by tectonic setting. (b) Distribution of the residuals for each tectonic setting. (c) Offsets from the global trend for each expedition (intercepts of random effect) estimated by the linear-mixed effect model, colored by tectonic setting. Vertical lines denote the 95% confidential interval. (d) Probability density function of residuals remaining after accounting for the effects of tectonic setting and expedition-specific offsets. (e) Proportion of the variance explained by each effect relative to the total variance.

approaches that integrate these sources with measured physical property data could provide more robust petrophysical interpretations without relying solely on machine learning predictions based on physical properties.

To identify the factors responsible for deviations from the global velocity–porosity trends, each drilling site was assgined to a tectonic setting and the influence of tectonic setting on these deviations was statistically evaluated its influence using LMM models. Although systematic shifts were observed among tectonic settings, their overall contribution was limited. Instead, regional differences among drilling sites and smaller-scale heterogeneity within individual sites had a much greater influences. However, the tectonic settings defined in this study represent proxies for multiple geological factors rather than individual geological processes. Consequently, the observed relationships and their interpretations may not isolate the effects of the tectonic setting and may overlook alternative classifications that more effectively explain the observed petrophysical variability. For sediments, factors such as sedimentation rate, distance from land, and water depth may independently influence physical properties, whereas for crustal rocks, the spreading rate and plate age may exert independent controls. The importance of such regional factors is also supported by the observation that differences among expeditions account for a large proportion of the variability in both sedimentary and basaltic datasets. Therefore, regional geological processes should be considered when interpreting physical property data, particularly when modeling velocity–porosity relationships, interpreting their fitted parameters, or applying such relationships to seismic velocity data to estimate the porosity and other petrophysical parameters.

Although more than half of the original data were excluded during quality control, if reliable measurements had been available for these samples, physical property trends associated with lithology and tectonic setting could potentially have been resolved in greater detail. Conversely, when using physical property data from drilling sites for which the available measurements included those that were excluded in the present study, the data quality should be carefully evaluated, particularly for MAD (density and porosity) data. Remeasurement and reanalysis of archived cores stored in core repositories may provide more robust constraints than were possible at the time of drilling. Such efforts would be particularly valuable if physical properties were measured together with geochemical, petrological, and other complementary properties on the same samples. This integrated approach could provide a stronger basis for linking petrophysical and geophysical observations to the geological processes of interest.

4 Conclusions

This study compiled legacy core data acquired over decades of scientific ocean drilling, including the ODP and IODP, to evaluate global variations in the physical properties of sediment and rock, with a particular emphasis on P-wave velocity–porosity relationships. Using a dataset from recent IODP expeditions in which physical property measurements are linked to lithological descriptions, I developed a machine learning model to predict simplified lithological classes from physical properties and applied it to legacy ODP/IODP data without lithological labels. The model successfully classified sedimentary and igneous lithologies with accuracies of 76%–96%, enabling us to identify lithology-dependent relationships among different physical properties. Distinct trends between physical properties were identified for each lithology, and different models were used to establish global velocity–porosity relationships for sediments and igneous rocks. For sediments, I applied a modified version of Erickson and Jarrard's (1998) model parameterized by consolidation index and shale/clay fraction, whereas the established differential effective medium (DEM) model was applied to igneous rocks. These models successfully reproduced the global velocity–porosity trends of sediments and crustal rocks, respectively. However, considerable scatter about the global trends was observed for all lithologies. A small amount of this variability was associated with the tectonic setting, whereas statistical analyses showed that most of the variability reflected differences among drilling areas in the same tectonic setting. Smaller-scale heterogeneity within individual drilling areas also contributed appreciably to the observed scatter. These results demonstrate that regional geological processes and local heterogeneity should be considered when interpreting the physical properties of sediment and rock, particularly when modeling velocity–porosity relationships, interpreting fitted model parameters, or applying such relationships to seismic velocity data to estimate porosity and other petrophysical parameters.

Acknowledgements

This study used data collected onboard the *JOIDES Resolution* during 155 expeditions operated by the Ocean Drilling Program (ODP), the Integrated Ocean Drilling Program (IODP), and the International Ocean Discovery Program (IODP). I thank the scientists, technicians, and crew who collected the data. This study used sCientific colour maps (Crameri, 2021).

Conflict of interest

The author declares no conflicts of interest relevant to this study.

Data availability statement

Data from the ODP and early IODP expeditions are available from the Janus and LIMS databases (https://www-odp.tamu.edu/database/; https://web.iodp.tamu.edu/LORE/). The LILY database is available via Zenodo(Childress et al., 2023, https://doi.org/10.5281/zenodo.8408297).

References

Akamatsu, Y., Nagase, K., Abe, N., Okazaki, K., Hatakeyama, K., & Katayama, I. (2023). Cross-property relationship between electrical resistivity and elastic wave velocity of crustal rocks from the oman drilling project hole GT3A: Implications for in situ geophysical properties of oceanic crust. *Journal of Geophysical Research, [Solid Earth]*, *128*. https://doi.org/10.1029/2022jb026130

Akamatsu, Y., Kuwatani, T., & Oyanagi, R. (2025). Alteration processes of mantle peridotite in the samail ophiolite inferred from independent component analysis of rock physical properties. *Lithos*, 107946. https://doi.org/10.1016/j.lithos.2025.107946

Akamatsu, Y., Fujii, M., Harigane, Y., Sakuyama, T., Yamamoto, Y., Kamiya, N., & Michibayashi, K. (2026). Cracked on-axis and pristine off-axis crust formed during forearc evolution at a nascent subduction zone. *Communications Earth & Environment*, *7*, 315. https://doi.org/10.1038/s43247-026-03400-7

Arculus, R. J., Gurnis, M., Ishizuka, O., Reagan, M. K., Pearce, J. A., & Sutherland, R. (2019). How to create new subduction zones. *Oceanography*, *32*, 160–174.

Berryman, J. G., Pride, S. R., & Wang, H. F. (2002). A differential scheme for elastic properties of rocks with dry or saturated cracks. *Geophysical Journal International*, *151*, 597–611. https://doi.org/10.1046/j.1365-246X.2002.01801.x

Blackman, D. K., Abe, N., Carlson, R. L., Guerin, G., Ildefonse, B., & Kumpf, A. (2019). Seismic properties of gabbroic sections in oceanic core complexes: Constraints from seafloor drilling. *Marine Geophysical Research*, *40*, 557–569. https://doi.org/10.1007/s11001-019-09385-7

Blum, P. (1997). *Physical properties handbook: A guide to the shipboard measurement of physical properties of deep-sea cores*. Ocean Drilling Program. https://doi.org/10.2973/odp.tn.26.1997

Brocher, T. M. (2005). Empirical relations between elastic wavespeeds and density in the earth's crust. *Bulletin of the Seismological Society of America*, *95*, 2081–2092. https://doi.org/10.1785/0120050077

Carlson, R. L. (2010). How crack porosity and shape control seismic velocities in the upper oceanic crust: Modeling downhole logs from holes 504B and 1256D. *Geochemistry, Geophysics, Geosystems*, *11*. https://doi.org/10.1029/2009gc002955

Carlson, R. L. (2014). The effects of alteration and porosity on seismic velocities in oceanic basalts and diabases. *Geochemistry, Geophysics, Geosystems: G(3)*, *15*, 4589–4598. https://doi.org/10.1002/2014gc005537

Cheng, C. H., & Toksöz, M. N. (1979). Inversion of seismic velocities for the pore aspect ratio spectrum of a rock. *Journal of Geophysical Research*, *84*, 7533–7543. https://doi.org/10.1029/jb084ib13p07533

Childress, L. B., Acton, G. D., Percuoco, V. P., & Hastedt, M. (2024). The LILY database: Linking lithology to IODP physical, chemical, and magnetic properties data. *Geochemistry, Geophysics, Geosystems*, *25*. https://doi.org/10.1029/2023gc011287

Christensen, N. I., & Salisbury, M. H. (1975). Structure and constitution of the lower oceanic crust. *Reviews of Geophysics (Washington, D.C.: 1985)*, *13*, 57–86. https://doi.org/10.1029/rg013i001p00057

Comas, M. C., Zahn, R., Klaus, A., & Leg 161 Shipboard Scientific Party (Eds.). (1996). *Proceedings of the ocean drilling program, 161 initial reports*. Ocean Drilling Program. https://doi.org/10.2973/odp.proc.ir.161.1996

Crameri, F. (2021). Scientific colour maps. computer software, Zenodo. https://doi.org/10.5281/ZENODO.5501399

D'Hondt, S., Inagaki, F., Orcutt, B. N., & Hinrichs, K. U. (2019). IODP advances in the understanding of subseafloor life. *Oceanography*, *32*, 198–207.

Erickson, S. N., & Jarrard, R. D. (1998). Velocity-porosity relationships for water-saturated siliciclastic sediments. *Journal of Geophysical Research*, *103*, 30385–30406. https://doi.org/10.1029/98jb02128

Fujii, M., Okino, K., Sato, H., Nakamura, K., Sato, T., & Yamazaki, T. (2016). Variation in magnetic properties of serpentinized peridotites exposed on the yokoniwa rise, central indian ridge: Insights into the role of magnetite in serpentinization. *Geochemistry, Geophysics, Geosystems*, *17*, 5024–5035. https://doi.org/10.1002/2016GC006511

Fulton, P. M., Brodsky, E., Mori, J. J., & Chester, F. M. (2019). TŌHOKU-OKI FAULT ZONE FRICTIONAL HEAT MEASURED. *Oceanography*, *32*, 102–104.

Hatakeyama, K., Katayama, I., Abe, N., Okazaki, K., & Michibayashi, K. (2021). Effects of alteration and cracks on the seismic velocity structure of oceanic lithosphere inferred from ultrasonic measurements of mafic and ultramafic samples collected by the oman drilling project. *Journal of Geophysical Research, [Solid Earth]*. https://doi.org/10.1029/2021jb021923

Heuer, V. B., Lever, M. A., Morono, Y., & Teske, A. (2019). The limits of life and the biosphere in earth's interior. *Oceanography*, *32*, 208–211.

Hoffman, N. W., & Tobin, H. J. (2004). An empirical relationship between velocity and porosity for underthrust sediments in the nankai trough accretionary prism. *Proc. Ocean Drill. Program Sci. Results, 190*, *196*, 1–23.

Jarrard, R. D., MacKay, M. E., Westbrook, G. K., & Screaton, E. J. (1995). Log-based porosity of ODP sites on the cascadia accretionary prism. In *Proceedings of the ocean drilling program, 146 part 1 scientific results*. Ocean Drilling Program. https://doi.org/10.2973/odp.proc.sr.146-1.249.1995

Jeppson, T. N., & Kitajima, H. (2022). Velocity-porosity relations in carbonate and siliciclastic subduction zone input materials. *Geochemistry, Geophysics, Geosystems: G(3)*, *23*, e2021GC010074. https://doi.org/10.1029/2021gc010074

Kachanov, M. (1994). Elastic solids with many cracks and related problems. In J. W. Hutchinson & T. Y. Wu (Eds.), *Advances in applied mechanics* (Vol. 30, pp. 259–445). Elsevier. https://doi.org/10.1016/S0065-2156(08)70176-5

Kelemen, P. B., Matter, J. M., Teagle, D. A. H., Coggon, J. A., & the Oman Drilling Project Science Team. (2020). *Proceedings of the oman drilling project*. International Ocean Discovery Program College Station, TX.

Koppers, A. A. P., & Coggon, R. (2020). *Exploring earth by scientific ocean drilling: 2050 science framework*. https://doi.org/10.6075/J0W66J9H

Kuster, G. T., & Toksöz, M. N. (1974). Velocity and attenuation of seismic waves in two-phase media: Part i. Theoretical formulations. *Geophysics*, *39*, 587–606. https://doi.org/10.1190/1.1440450

Le Ber, E., Loggia, D., Denchik, N., Lofi, J., Kring, D. A., Sardini, P., et al. (2022). Petrophysics of chicxulub impact crater's peak ring. *Journal of Geophysical Research. Solid Earth*, *127*, e2021JB023801. https://doi.org/10.1029/2021jb023801

Lee, E. Y., Tejada, M. L. G., Song, I., Chun, S. S., Gier, S., Riquier, L., et al. (2021). Petrophysical property modifications by alteration in a volcanic sequence at IODP site U1513, naturaliste plateau. *Journal of Geophysical Research, [Solid Earth]*, *126*, e2020JB021061. https://doi.org/10.1029/2020JB021061

Littler, K., Westerhold, T., Drury, A. J., Liebrand, D., Lisiecki, L., & Pälike, H. (2019). Astronomical time keeping of earth history: An invaluable contribution of scientific ocean drilling. *Oceanography*, *32*, 72–76. https://doi.org/10.5670/oceanog.2019.122

Lowery, C. M., Morgan, J. V., Gulick, S. P., Bralower, T. J., & Christeson, G. L. (2019). Ocean drilling perspectives on meteorite impacts. *Oceanography*, *32*, 120–134.

Mavko, G., Mukerji, T., & Dvorkin, J. (2020). *The rock physics handbook*. Cambridge University Press.

Michibayashi, K., Tominaga, M., Ildefonse, B., & Teagle, D. (2019). What lies beneath: The formation and evolution of oceanic lithosphere. *Oceanography*, *32*, 138–149. https://doi.org/10.5670/oceanog.2019.136

Miller, D. J., & Christensen, N. I. (1997). Seismic velocities of lower crustal and upper mantle rocks from the slow-spreading mid-atlantic ridge, south of the kane transform zone (MARK). In *Proceedings of the ocean drilling program, 153 scientific results* (pp.

437–456). Ocean Drilling Program. https://doi.org/10.2973/odp.proc.sr.153.043.1997
Nakagawa, S., & Schielzeth, H. (2013). A general and simple method for obtainingR2from generalized linear mixed-effects models. *Methods in Ecology and Evolution*, *4*, 133–142. https://doi.org/10.1111/j.2041-210x.2012.00261.x
Neal, C. R., Coffin, M. F., & Sager, W. W. (2019). Contributions of scientific ocean drilling to understanding the emplacement of submarine large igneous provinces and their effects on the environment. *Oceanography*, *32*, 176–192.
Nur, A. M., Mavko, G., Dvorkin, J., & Gal, D. (1995). Critical porosity: The key to relating physical properties to porosity in rocks. *1995 SEG Annual Meeting*, SEG-1995-0878.
O'Connell, R. J., & Budiansky, B. (1974). Seismic velocities in dry and saturated cracked solids. *Journal of Geophysical Research*, *79*, 5412–5426. https://doi.org/10.1029/jb079i035p05412
Oufi, O., Cannat, M., & Horen, H. (2002). Magnetic properties of variably serpentinized abyssal peridotites. *Journal of Geophysical Research, [Solid Earth]*, *107*, EPM 3-1-EPM 3-19. https://doi.org/10.1029/2001JB000549
Salisbury, M. H., Shinohara, M., Richter, C., & Leg 195 Shipboard Scientific Party (Eds.). (2002). *Proceedings of the ocean drilling program, 195 initial reports*. Ocean Drilling Program. https://doi.org/10.2973/odp.proc.ir.195.2002
Svadlenak, H., Parnell-Turner, R., & Morris, M. (2026). A global evaluation of lithology-dependent marine sediment compaction parameters and their uncertainties. *Geochemistry, Geophysics, Geosystems: G(3)*, *27*, e2025GC012739. https://doi.org/10.1029/2025gc012739
Swift, S., Reichow, M., Tikku, A., Tominaga, M., & Gilbert, L. (2008). Velocity structure of upper ocean crust at ocean drilling program site 1256. *Geochemistry, Geophysics, Geosystems*, *9*. https://doi.org/10.1029/2008gc002188
Takei, Y. (2002). Effect of pore geometry onVP/VS: From equilibrium geometry to crack. *Journal of Geophysical Research*, *107*. https://doi.org/10.1029/2001jb000522
Teagle, D. A. H., Alt, J. C., Umino, S., Miyashita, S., Banerjee, N. R., Wilson, D. S., & Crispini, L. (2006). *Proceedings of the integrated ocean drilling program, volume 309/312* (Vol. 309–312, pp. 1–549). Integrated Ocean Drilling Program. https://doi.org/10.2204/iodp.proc.309312.2006
Tsuji, T., & Iturrino, G. J. (2008). Velocity-porosity relationships in oceanic basalt from eastern flank of the juan de fuca ridge: The effect of crack closure on seismic velocity. *Exploration Geophysics*, *39*, 41–51. https://doi.org/10.1071/EG08001
Tsuji, T., Tokuyama, H., Costa Pisani, P., & Moore, G. (2008). Effective stress and pore pressure in the nankai accretionary prism off the muroto peninsula, southwestern japan. *Journal of Geophysical Research*, *113*. https://doi.org/10.1029/2007jb005002
Violay, M., Pezard, P. A., Ildefonse, B., Belghoul, A., & Laverne, C. (2010). Petrophysical properties of the root zone of sheeted dikes in the ocean crust: A case study from hole ODP/IODP 1256D, eastern equatorial pacific. *Tectonophysics*, *493*, 139–152. https://doi.org/10.1016/j.tecto.2010.07.013
Wang, H.-M., Wang, W.-H., Doan, M.-L., & Tang, X.-M. (2026). The power-law characteristics in the microcrack system of a rock: Inversion and analysis of laboratory velocity–pressure data. *Geophysical Journal International*, *247*, ggag302. https://doi.org/10.1093/gji/ggag302
Wefer, G., Berger, W. H., Richter, C., & Leg 175 Shipboard Scientific Party (Eds.). (1998). *Proceedings of the ocean drilling program 175 initial reports*. Ocean Drilling

Program. https://doi.org/10.2973/odp.proc.ir.175.1998